

Seismic resurfacing of 433 Eros indicative of a highly dissipative interior for large near-Earth asteroids

Received: 2 October 2023

Accepted: 9 October 2024

Published online: 15 November 2024

 Check for updatesR.-L. Ballouz^{1,5}✉, C. M. Ernst^{1,5}, O. S. Barnouin¹, R. T. Daly¹,
D. N. DellaGiustina², B. A. Hyatt^{3,4} & A. C. Martin¹

An asteroid's interior dictates how its space environment changes its shape and surface, which provides a record of the collisional and dynamical evolution of the Solar System. Knowledge of asteroid interiors also enables the formulation of mitigation strategies against hazardous asteroids. Despite this importance, asteroid interiors remain poorly understood. Asteroids between 0.2 km and 10 km in diameter are thought to have rubble-pile interiors, transitioning to fractured interiors at 10 km scales, then to coherent and differentiated interiors at ≥ 100 km scales. The asteroid 433 Eros, the only 10-km-scale asteroid explored by a rendezvous mission, is an exemplar of asteroids at intermediate scales. Recent exploration of smaller rubble piles has provided insight into physical properties that are shared with Eros-sized objects. Here we quantify the seismic and physical properties of Eros' interior through measurements and modelling of crater degradation and erasure from the impact that formed the 7.5-km-diameter Shoemaker crater on Eros. Our results indicate that Eros' deep interior has a seismic wave scattering length of 0.5 ± 0.1 km and effective quality factor $^EQ < 63^{+18}_{-13}$ at frequencies > 0.06 Hz. Contrary to the established view of Eros as a fractured shard, our findings suggest that Eros' interior properties are consistent with those of a rubble-pile asteroid.

While never directly measured, the interior properties of asteroids have been inferred through analyses of their impact craters, spin properties and gravitational dynamics^{1–7}. 433 Eros is an elongated $34 \text{ km} \times 11 \text{ km} \times 11 \text{ km}$ near-Earth asteroid (NEA) that was visited by the Near Earth Asteroid Rendezvous (NEAR) mission, which obtained global imaging coverage of the asteroid with its Multi-Spectral Imager (MSI)⁸. As Eros is the only 10-km-scale asteroid to be visited by a rendezvous space mission, NEAR data enable the detailed study of the connection between surface processes and hypothesized interiors for intermediate-size (10–100 km) asteroids^{3–5}.

MSI revealed a regolith-covered surface on Eros that is heavily cratered at > 1 km scales⁹. Eros has three large impact craters that dominate its shape: Himeros (9.7 km diameter), Shoemaker (7.5 km diameter) and Psyche (5.6 km diameter). Shoemaker is thought to be the youngest of these craters, based on its superposition of Himeros and the distribution of boulders and craters in its vicinity⁹. Geologic interpretation of MSI images of the Eros surface suggests that its interior is heavily fractured yet coherent, indicated by craters that appear to form with structural control⁵, surface lineaments¹⁰ and its estimated macroporosity of 16–19% (refs. 11–15).

More recent spacecraft observations of smaller kilometre-scale NEAs^{16–18} indicate 'rubble-pile' interiors that are different from fractured

¹Johns Hopkins University Applied Physics Lab, Laurel, MD, USA. ²Lunar and Planetary Lab, University of Arizona, Tucson, AZ, USA. ³Northwestern University, Evanston, IL, USA. ⁴University of Maryland, Baltimore County, Baltimore, MD, USA. ⁵These authors contributed equally: R.-L. Ballouz, C. M. Ernst. ✉e-mail: ronald.ballouz@jhuapl.edu

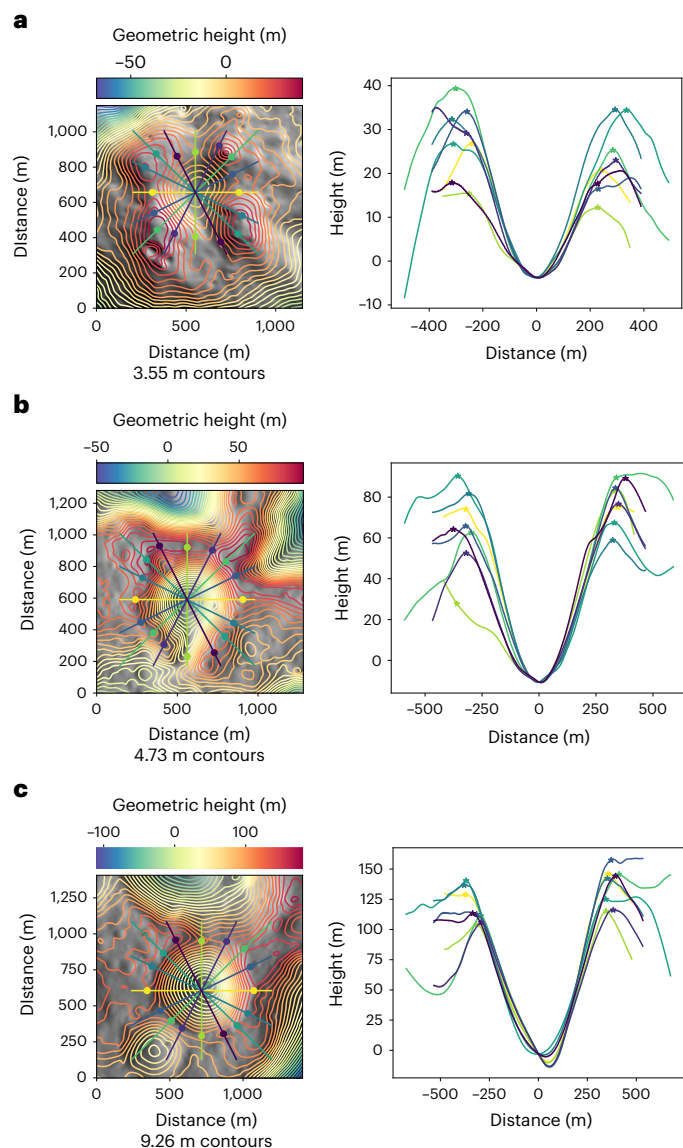


Fig. 1 | Eros exhibits a diversity in crater morphology. **a–c**, Examples of local DTMs of Eros craters (contour maps of geometric height, left) and their measured profiles (right): an example of a shallow crater, CRT328 (65° S, 19° E), $d/D = 0.056 \pm 0.016$ (**a**); an example of a crater with average d/D , CRT210 (3° N, 310° E), $d/D = 0.130 \pm 0.011$ (**b**); an example of a deep crater CRT095 (32° S, 225° E), $d/D = 0.205 \pm 0.020$ (**c**). Eight profiles, with origins at the crater centre and equally spaced in the azimuthal direction, are used to obtain a robust measurement of crater morphology. Each profile has two asterisks that mark the positions of the crater rim.

shards. A rubble pile is a gravitational aggregate that is hypothesized to have been sourced from the catastrophic disruption of a larger 100-km-scale parent body that creates an asteroid family⁴. The rubble-pile nature and collisional origin of these kilometre-scale NEAs is supported by analysis of returned samples^{19,20} and measurements of their rotation periods²¹.

Asteroids larger than 10 km, like Eros, are thought to be sufficiently large that solar radiative torques and collisions could not disrupt them in timescales smaller than the age of the Solar System⁴. Hence, it is plausible that intermediate-size asteroids are primordial and preserve their original, albeit fractured, coherent interiors. However, intermediate-size asteroids have been observed to be part of asteroid families²², suggesting that some may be rubble-pile products of catastrophic disruption events. Furthermore, bulk density measurements of kilometre-scale NEAs

indicate that their macroporosities may be lower than those estimated for Eros^{7,23}.

Therefore, analyses of Eros' interior and structural properties could provide a conceptual bridge for understanding the relationship between 100 km planetesimal parent bodies and the kilometre-scale NEAs: are intermediate-size asteroids also rubble piles formed from the catastrophic disruption of a 100 km parent body, or are they fractured shards that persevered an inherently primordial interior structure? A detailed quantitative understanding of intermediate-scale asteroid interior informs asteroid crater chronologies, which capture the dynamical history of the inner Solar System⁴. Furthermore, the dissipative qualities of the asteroid interior also determine how multi-component asteroid systems evolve through tidal forcing², and contribute to formulating mitigation strategies against hazardous asteroids²⁴.

We consider the crater population of Eros to probe its interior properties. Previous work has shown that Eros exhibits a global deficiency in small craters⁸, with craters <200 m depleted relative to predicted empirical saturation. Depletion of small crater populations has also been observed on smaller NEAs¹⁸. On the basis of Eros' hypothesized coherent interior structure, ref. 25 argues qualitatively that body seismic waves generated by the Shoemaker-forming impact could have caused regional resurfacing on Eros. In contrast, ref. 26 used numerical models of impact-induced global seismicity, assuming lunar mega-regolith-like seismic properties for Eros, to argue that crater degradation on Eros proceeds through the cumulative effect of its impact history. Therefore, it is unclear whether seismic shaking on fractured 10-km-scale asteroids leads to global^{26,27} or regional²⁵ resurfacing, as quantitative knowledge of asteroid interior and seismic properties is unknown. Through a detailed morphological assessment of Eros' craters, we study crater degradation and erasure on Eros without making a priori assumptions of its interior structure properties.

Spatial relationships of crater properties and Shoemaker

We measured the depths and diameters of craters (≥ 240 m in diameter, and complete to 550 m) by creating high-resolution (3 m ground sample distance) digital terrain models (DTMs) using co-registered high-resolution images from MSI and a high-resolution stereophotoclinometry (SPC) shape model of Eros²⁸ (Fig. 1). The accuracy of the DTMs was confirmed by comparison with topographic data from the NEAR Laser Rangefinder (NLR) ('Crater shape models' section in Methods). The SPC model enables global crater morphology measurements as it is not limited by illumination conditions (for shadow-based measurements on individual images) or the alignment of an NLR track with a crater centre.

We find that the global mean d/D ratio for craters in our survey is 0.12 ± 0.03 (Extended Data Fig. 1a). This value is small compared with an 'ideal' fresh lunar crater ratio of 0.2 (ref. 29); however, it is close to the mean d/D value on other asteroids (~ 0.15 ; ref. 30). There is a larger spread in d/D values at smaller sizes, and craters 500–1,000 m in diameter exhibit the largest degree of degradation (Extended Data Fig. 1b). The minimum d/D measured was 0.05 ± 0.01 (Crater430), although shallower craters may be difficult to identify. The maximum d/D measured was 0.23 ± 0.01 (Crater017).

A spatial analysis of our crater morphology measurements reveals that the median d/D of craters with $D > 500$ m increases with distance to Shoemaker crater (Fig. 2a), before reaching a median saturation value of ~ 0.12 at distances of ~ 10 km. A similar analysis for smaller ($D < 500$ m) craters found no clear trend (Extended Data Fig. 1c). Furthermore, no other clear trend of d/D with distance from the other large craters on Eros ($D > 2$ km) is apparent (Extended Data Fig. 2).

Previous studies of Eros have shown that the large boulder population (> 30 m diameter) probably tracks ejecta from Shoemaker crater³¹, and the relative crater density is shallowest in a region surrounding the

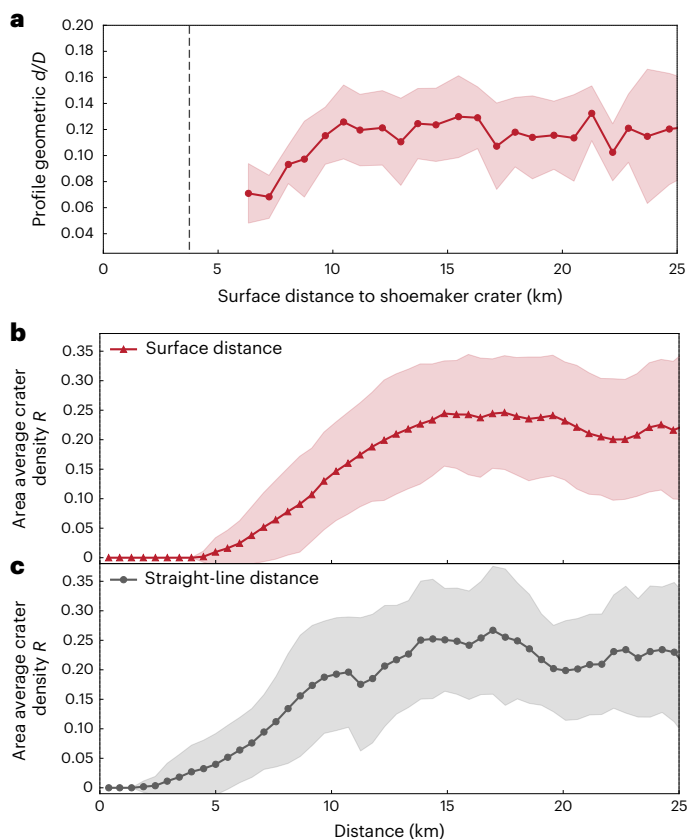


Fig. 2 | The depth-to-diameter ratios of large craters and the spatial density of all craters increase with distance from Shoemaker crater. a, The geometric d/D of craters increases as a function of distance from the centre of Shoemaker crater for craters with $D > 500$ m, up to a distance of ~10–12 km. The red curve shows the moving average (median) of d/D at a bin size of 0.8 km. The vertical dashed black line marks one Shoemaker crater radius. **b,** The area average crater density R , of craters with $D = 500$ –2,000 m also increases as a function of surface (geodesic, red curve with triangles) distance from the centre of Shoemaker crater. **c,** The same as **b**, except for straight-line (Euclidean, grey curve with circles, similar to Fig. 2b of ref. 25) distance. The shaded region in each subpanel represents the 1-sigma standard deviation centred on each bin.

same crater²⁵. In Fig. 2b,c, we used a shape model of Eros with a mean facet length of 150 m (ref. 28) to reproduce the analysis of ref. 31 showing the increase in the area average crater density R (the mean crater density within $2 \text{ km} \times 2 \text{ km}$ bins for craters with $D = 0.5$ –2 km) as a function of straight-line distance from the centre of Shoemaker crater (grey curve with circles). We also show how crater R varies with the surface distance from Shoemaker crater (red curve with triangles), which we define as the shortest distance along the surface to Shoemaker crater (that is, the geodesic). We find that the median values of both crater R and d/D increase with distance to Shoemaker crater; however, both crater properties asymptote at larger values of surface distance compared with straight-line distances (Fig. 2b,c and Extended Data Fig. 3).

These trends are more clearly visualized in shape-model-projected data of crater properties and their spatial relationship to Shoemaker crater (Fig. 3), where each facet is coloured on the basis of the median value of each property within a 2 km radius. We mapped a continuous region of shallow craters that surrounds Shoemaker (Fig. 3, magenta polygon). We term this region the Shallow Crater Region of Eros, which makes up ~20% of Eros' surface area. Figure 3f highlights the Shoemaker-crater antipode, where a chevron pattern of crater depletion is apparent for craters with $D = 0.177$ –1 km, noted by ref. 25 as possible evidence for a seismic resurfacing event generated by the Shoemaker-forming impact. We note that this chevron pattern disappears when only large craters are considered ($D = 0.5$ –2 km).

Here, we do not find a similar spatial pattern emerging in the d/D data (compare Fig. 3b,f).

In Fig. 4, we compare crater R size frequency distribution globally and for two regions of interest (ROIs): the Shoemaker antipode (marked by the chevron shape in Fig. 3f) and the Shallow Crater Region. From Fig. 4, we see that the Shallow Crater Region has a clear paucity of craters compared with both the global population and the Shoemaker antipode. Indeed, the Shoemaker antipode's crater R looks markedly similar to the global population at $D > 600$ m, and there is a higher crater density compared with the Shallow Crater Region for $D > 250$ m.

The marked difference in crater R and d/D in the two ROIs is surprising because both regions extend to approximately equivalent straight-line distances from the centre of Shoemaker crater. If body seismic waves generated from the Shoemaker-forming impact were the dominant source for global resurfacing, then one could expect a similar degree of surface changes within the two ROIs. Therefore, alternative mechanisms, such as crater ejecta, probably play a role in crater erasure and degradation from the Shoemaker-forming impact.

Ejecta contributions to crater erasure and degradation

To investigate the relative contribution of crater ejecta deposition on the d/D , we performed a series of direct N -body simulations that tracked the fate of Shoemaker crater ejecta. We used the N -body collisional code pkdgrav³² combined with empirical scaling relationships for the velocity distribution of ejecta following a hypervelocity impact ('pkdgrav simulations of the fate of Shoemaker ejecta' section in Methods). Figure 5 shows snapshots from one of the pkdgrav simulations (Supplementary Video 1) for case 1 in Extended Data Table 2.

By tracking ejecta that are deposited across Eros, we measure the total change in depth across different regions (Fig. 3i–l). We find that the volume of ejecta may not be sufficient to explain the degradation of most craters immediately surrounding Shoemaker crater, but it may explain the depletion of small craters (<500 m) at the antipode (Supplementary Information). We find that the simulations consistently produce ejecta patterns with a chevron shape at the antipode (Fig. 3j). This pattern emerges due to Eros' unique shape, with some contribution from its spin state (Eros is a relatively fast principal axis rotator with a spin period of 5.27 h). Material that is ejected westwards has a relatively short path to the antipode, leading to a chevron shape upon reimpact. Analysing the depth of ejecta required to erase craters (Supplementary Information), we find that Shoemaker ejecta may have been sufficient to erase the small crater population ($D < 250$ m) at the antipode, while keeping the large crater population ($D > 500$ m) relatively undegraded, which may explain the mismatch in spatial patterns of the antipode between the maps of crater R and d/D in Fig. 3b,f.

Seismic shaking contributions to crater erasure and degradation

To investigate the limited observable extent of seismic effects from Shoemaker crater's formation, we combined our measurements of crater d/D in the vicinity of Shoemaker crater with a first-principles analysis of seismic wave propagation³³ and using the mathematical descriptions for crater degradation through regolith downslope diffusion ('Crater degradation model' section in Methods). As we have shown that craters with $D > 500$ m up to a surface distance of ~12 km of Shoemaker crater were probably degraded by Shoemaker's formation, we isolate these craters and measure the magnitude of downslope material diffusion, K , required to degrade each crater to its observed state ('Crater degradation model' section in Methods). We find a clear decrease in K as a function of surface distance (Fig. 4b) and model this decay through the propagation of a surface seismic wave from the centre of Shoemaker.

In 'Seismic wave decay model' section in Methods, we show that, under the assumption of a strongly scattering medium, the decay in

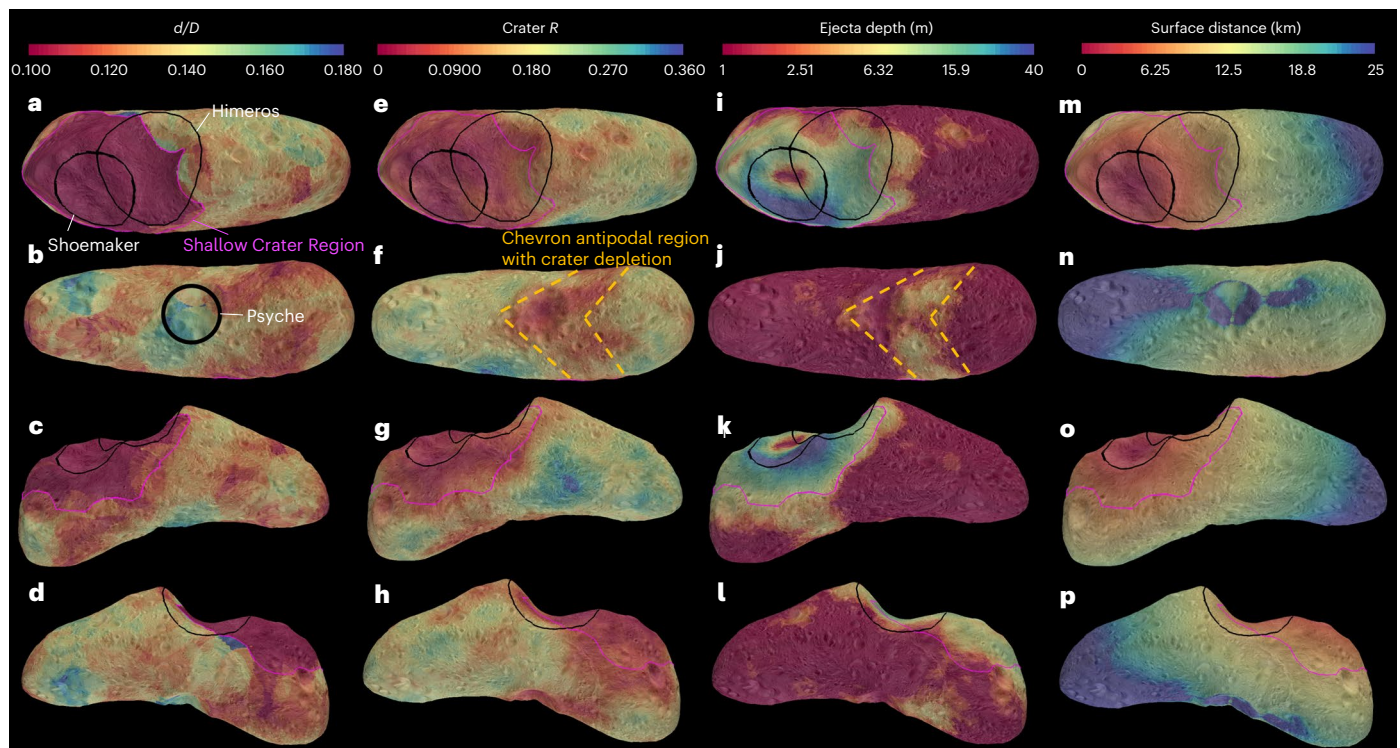


Fig. 3 | Spatial relationships exist between crater properties, the deposition of Shoemaker ejecta and the surface distance from Shoemaker. The d/D , crater R , modelled Shoemaker ejecta depth and surface distance from Shoemaker crater are projected onto an Eros shape model generated using the Small Body Mapping Tool (SBMT)⁶³, shown with a projected basemap of Eros⁶⁴. Each facet represents the median value in a $2\text{ km} \times 2\text{ km}$ bin. Both d/D and crater R are at a minimum in a region surrounding Shoemaker crater. **a–d**, Four views of the area average d/D of craters on Eros: centred on (0° N , 90° E) (**a**), centred on (0° N , 270° E) (**b**), centred on the southern pole (**c**) and centred on the northern pole (**d**). North is up in **a** and **b**. The Shallow Crater Region is outlined in magenta. **e–h**, Similar views of Eros as shown in **a–d**, respectively, but with the crater R

of Eros' surface shown for craters that have $D = 0.177\text{--}1\text{ km}$ (similar to fig. 1 of ref. 25). The antipodal region of Shoemaker crater (shown in the second row) (**f**) exhibits a chevron shape region with small values of crater R . **i–l**, Similar views of Eros as shown in **a–d**, respectively, but with the ejecta depth shown. Ejecta depth is calculated from numerical simulations of ejecta deposition using pkdgrav. The ejecta depth is largest on the southern rim of Shoemaker, but the values are not large enough to explain the observed crater degradation. However, ejecta deposition may explain the decrease in crater R at the antipodal region (**h**), as the simulations reproduce the chevron pattern. **m–p**, Similar views of Eros as shown in **a–d**, respectively, but with the surface distance from the centre of Shoemaker crater shown.

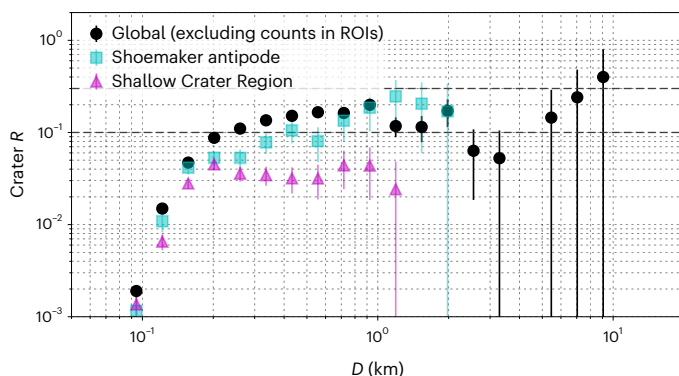


Fig. 4 | Crater erasure from the Shoemaker-forming impact was most efficient in the Shallow Crater Region that surrounds Shoemaker. Crater R for the global surface excluding crater counts in the ROIs (black circles), the Shoemaker antipode region (cyan squares) and the Shallow Crater Region (magenta triangles). The horizontal dashed black lines show the range for crater saturation (0.1–0.3). The data points represent the mean crater R and the 1-sigma standard deviation assuming Poisson statistics. The Shallow Crater Region exhibits a strong depletion of craters at all sizes compared with the global population of craters that excludes the ROIs. In contrast, the Shoemaker antipode is saturated with craters for $D > 300\text{ m}$.

the energy density of Rayleigh surface waves with distance is parameterized by only the scattering length, L_s , which describes the mean free path of seismic waves as they diffuse from the source. Therefore, the value of L_s for the Eros interior can be measured using our fit to

the K versus surface distance to Shoemaker data (Fig. 4b), and we find $L_s = 0.5 \pm 0.1\text{ km}$. Our modelled decay of K as a function of distance provides insights into the limited contribution of seismic shaking to global resurfacing and crater erasure on Eros. For a given value of K , the maximum crater size that could be erased by downslope diffusion can be determined ('Crater degradation model' section in Methods). In the Shallow Crater Region, which extends out to a surface distance of 10 km, our model predicts the complete erasure of craters with $D < 250\text{--}350\text{ m}$ (Extended Data Figs. 4 and 5, and Supplementary Information). Here, we define complete erasure as the point at which a crater has a sufficiently shallow d/D that it can no longer be detected in the data products at hand. A surface wave would only erase $<70\text{-m}$ -diameter craters in the antipodal region (a surface distance of $>20\text{ km}$). Extended Data Table 1 summarizes how the combination of ejecta and seismic surface waves can explain crater observations and highlights the diminished contribution of seismic body waves to regional resurfacing.

Our solution is similar to the scattering length of lunar regolith (on the order of $0.1\text{--}0.3\text{ km}$)³⁴ and that determined for Eros from statistical analysis of global crater erasure on Eros through the effect of its cumulative impact history ($0.25\text{--}1\text{ km}$)²⁷. Here, the impact that formed Shoemaker crater excited surface seismic waves that probe deep into the Eros interior (up to $\sim 5\text{ km}$ from the surface; Supplementary Information). Furthermore, unlike prior studies of resurfacing on Eros²⁶ that assumed lunar-like mega-regolith properties for the Eros interior, this solution suggests that the interior is highly dissipative, where the effective quality factor $Q \ll 1,000$.

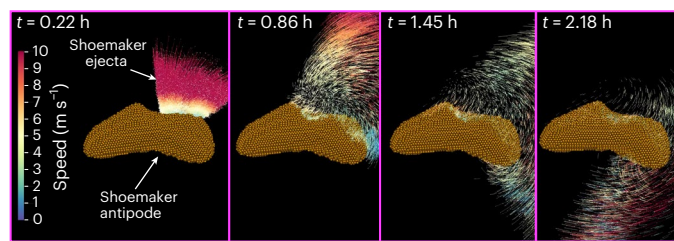


Fig. 5 | *N*-body simulations show that ejecta from the Shoemaker-forming impact are emplaced on the antipode. Snapshots of a pdgrav simulation (case 1; Extended Data Table 2) in a 5.27-h-period rotating frame showing the evolution of ejecta and its reimpact on a pdgrav model of Eros (brown rigid body) over the course of -0.5 of an Eros spin period from time $t = 0.28$ to 2.18 h

after impact. Ejecta are able to be emplaced onto the antipode with a clear preference for the region west of Psyche crater owing to the irregular shape of Eros. The antipodally emplaced ejecta form a chevron-shaped pattern (Fig. 3j). Supplementary Video 1 shows an animated visualization of this simulation.

In combination, our modelling and observations suggest that a body seismic wave could not have caused widespread resurfacing on Eros, as proposed by ref. 25 (Supplementary Information and Extended Data Table 1). Instead, the marked difference in crater R and d/D in the two ROIs indicates that a combination of mechanisms contributed to their resurfacing: surface seismic waves and ejecta.

Constraints on quality factor

Given the lack of any observable resurfacing at the antipode that can be directly attributed to body seismic waves, we can use our solution for L_s to constrain the seismic quality factor of the interior, at the seismic frequencies excited by the Shoemaker-forming impact. As the seismic properties of the Eros deep interior are unknown (such as compressional wave speed, V_p , and seismic efficiency, η), we model the diffusion of seismic body waves with straight-line distance using two different models for the interior: (1) a heavily fractured but coherent interior that is weakly scattering and where attenuation is parameterized by an intrinsic seismic quality factor, iQ_s , and (2) a rubble-pile interior that is strongly scattering (Fig. 6b and Supplementary Information).

Using a Monte-Carlo analysis that varied V_p and $\eta = 10^{-4}$ – 10^{-6} (ref. 35), we evaluate how seismic accelerations, a , attenuate with distance until they are equivalent to the mean gravity on Eros, g , which we define as the resurfacing limit²⁶. We find that body seismic waves are attenuated below the resurfacing limit for the heavily fractured model for an upper limit of $^iQ_s = 63^{+18}_{-13}$ (1-sigma uncertainties; Fig. 6c). Evaluating the seismic source duration for the Shoemaker-forming impact indicates that this is the value of the quality factor for seismic cut-off frequencies, ω_s , >0.06 Hz. Characteristic frequencies for the body waves generated by this impact are on the order of 2 Hz. We note that a rubble-pile interior would attenuate a/g at distances <3 km for a range of reasonable assumptions for η . In comparison, laboratory measurements of porous sandstone and granite are $^iQ_s \approx 60$ and 250, respectively; however, those measurements are made at frequencies higher than the seismic frequencies involved with the Shoemaker impact³⁶. Values of $^iQ_s \approx 60$ at $\omega_s = 0.1$ – 1 Hz have never been directly measured on planetary surfaces but are closer to values of the scattering loss quality factor measured for the lunar mega-regolith³⁷. This surprisingly low value for the iQ_s solution suggests that the attenuation of body waves may be dominated by scattering losses, such that the scattering quality factor dominates over an intrinsic quality factor. Thus, our solution may more accurately reflect an upper limit for the effective quality factor of the Eros interior, eQ_s .

Our results place new constraints on the dissipative properties of an asteroid's interior, which has never been directly characterized. On the basis of the tidal evolution of planetary satellites, ref. 38 suggest that asteroid monoliths may have tidal quality factors $Q_T \approx 100$ at tidal periods of ~ 10 – 100 h or tidal frequency $\omega_T \approx 10^{-4}$ – 10^{-5} (common for solar system satellites) and that rubble piles should have much smaller Q_T , although precisely how much smaller is unknown.

For larger planetary bodies, eQ has been scaled to a value of Q_T using the following relationship: $Q_T = ^eQ (\omega_T/\omega_s)^\gamma$, where $\gamma = 0.2$ – 0.33 (refs. 39,40). For rubble piles, the scaling from eQ to Q_T may be valid if tidal dissipation is also driven by the interaction of individual elements, which is the source of seismic scattering, as hypothesized by refs. 2,38.

Using the range of γ defined above, our modelling would indicate that a rubble-pile Eros would have $Q_T < 5$ – 22 . This upper limit for Q_T is up to an order of magnitude smaller than had been previously measured for the 100 km asteroid Kleopatra, on the basis of tidal lag measurements⁴¹, but these values are consistent with tidal quality factors for rubble piles determined through direct numerical simulations⁴².

Discussion

The results of our analyses suggest a different model for the Eros interior compared with prior studies that argued for a coherent but fractured interior^{25–27}. Given that the effective quality factor of Eros' interior is most similar to the scattering quality factor of planetary regolith³⁷, our analysis suggests that Eros is a rubble pile or, at the very least, the Eros interior responds to exterior stresses similar to a rubble pile. However, we caution that a rubble-pile interior model for Eros would be fundamentally different than what is commonly envisioned for smaller kilometre-scale rubble piles visited by spacecraft^{16–18}. For Eros, the scattering length solution, $L_s = 0.5 \pm 0.1$ km, suggests that the Eros interior contains large blocks that may span the entirety of the smaller kilometre-scale asteroids. Furthermore, we expect that the value of L_s should naturally scale with asteroid size, with smaller rubble piles having shorter seismic scattering lengths as they are composed of smaller blocks. Therefore, kilometre-scale NEAs would have more strongly attenuating interiors. We note that this work only approximately models the decay of seismic waves, neglecting geometric effects such as antipodal focusing. Given the apparently strongly scattering nature of the Eros surface, as indicated by our analyses, we do not foresee antipodal focusing of surface waves as an important contributor. Our model predicts a relatively small scattering length for surface seismic waves compared with the tortuous paths that surface waves would need to take to reach the antipode (up to ~ 60 km). However, we do foresee that future detailed geometric modelling of seismic wave propagation⁴³ applied to Eros could potentially provide better constraints on Eros internal properties.

Previous work pointed to surface expressions of subsurface strength on Eros, such as surface lineaments¹⁰, as evidence for a 'fractured-shard' nature. Lineaments on rubble piles can be the result of a weakly cohesive layer existing below the top-most cohesionless regolith layer. Furthermore, ref. 10 showed that the largest set of lineaments on Eros pre-date its largest craters, suggesting active resurfacing on a relatively weak body, or structure inherited from the gravitational reaccretion event that led to the formation of Eros. Linear features on the Martian moon Phobos have been demonstrated to form through the tidal deformation of the small body that leads to the opening of drainage

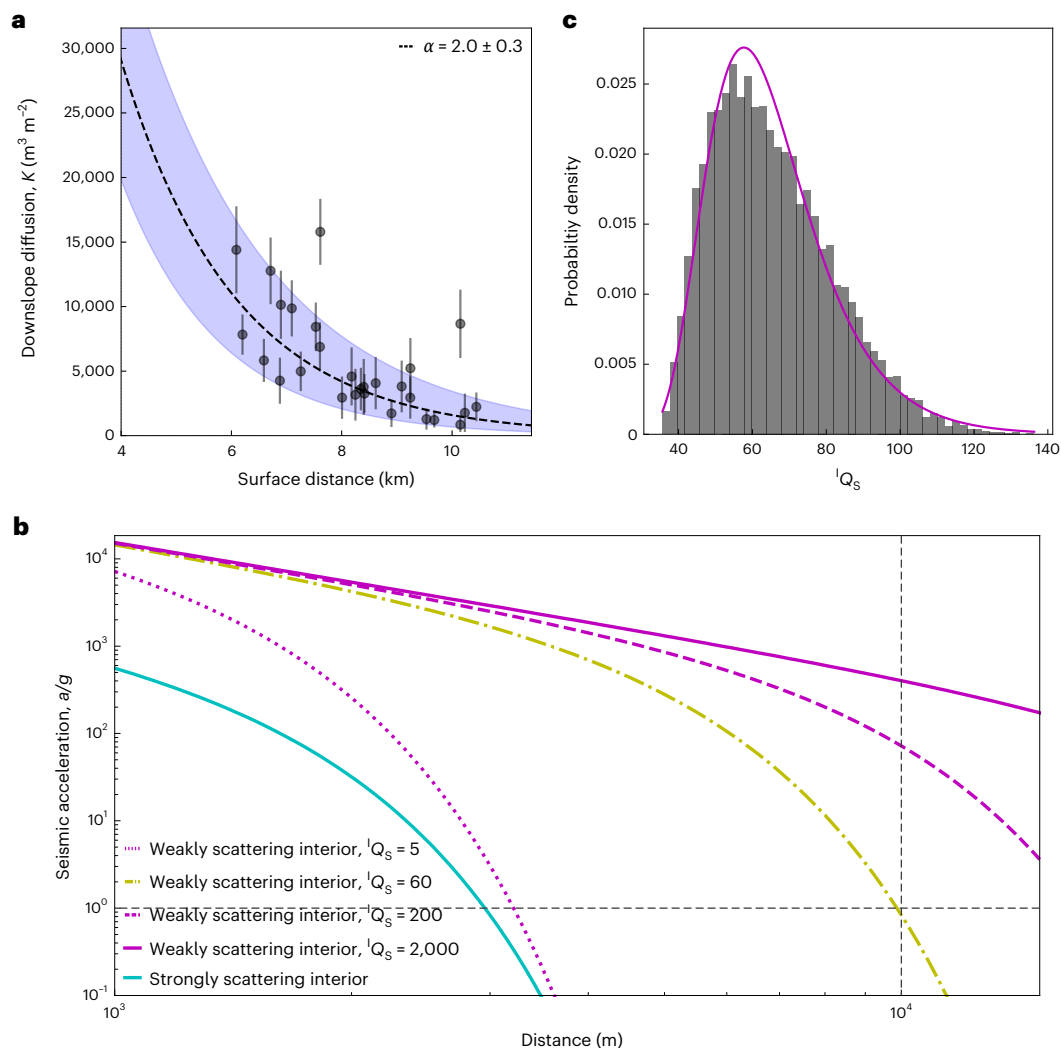


Fig. 6 | Modelling the degradation of craters from seismic waves induced by the Shoemaker-forming impact indicates that the Eros interior is highly dissipative. a, For each crater within 10 km of the centre of Shoemaker crater (black dots), the downslope diffusion constant, K , needed for the crater to evolve from an initial d/D to its current d/D . The best-fit solution to the decay of the surface seismic wave (dashed curve) gives $\alpha = 2.0 \pm 0.3$ km. The shaded blue region denotes 1-sigma uncertainty that is centred on the best-fit curve. The data points represent the mean $K \pm 1$ standard deviation based on $N = 50$ Monte-Carlo samples. **b**, The surface acceleration due to body seismic waves with distance from the impact point for $L_s = 0.5$ km, $\eta = 10^{-5}$ and $V_p = 3$ km s $^{-1}$. The solid, dashed

and dotted magenta curves show a/g for $Q_s = 2,000, 200$ and 5 , respectively. The dot-dashed yellow curve shows a/g for $Q_s = 60$, where $a/g = 1$ (dotted horizontal black line) when distance, $r = 10$ km (dotted vertical black line). The cyan curve shows a/g for a strongly scattering interior. **c**, The distribution of solutions for the upper limit of Q_s from a Monte-Carlo simulation ($N = 10,000$ samples) that varied $L_s = 0.5 \pm 0.1$ km (normally distributed), $\eta = 10^{-4}$ – 10^{-6} (uniformly distributed) and $V_p = 1$ – 5 km s $^{-1}$ (uniformly distributed). The solutions (histogram) are well represented by a lognormal distribution (magenta curve). The solutions have a median value of $Q_s = 63^{+18}_{-13}$, where the uncertainty reflects the 1-sigma confidence interval.

grooves in subsurface cohesive layers of a rubble-pile interior⁴⁴, which can be sustained in low-gravity environments with a relatively small magnitude of inter-particle cohesion. References^{3,45} have shown that layering may also be present on smaller NEAs such as Benu.

A rubble-pile interior for Eros would be consistent with theories for the formation of NEAs through catastrophic disruption of 100 km parent bodies. Our findings imply that (1) all second-generation-or-later asteroids may be rubble piles, regardless of size, and (2) that an Eros parent body must exist somewhere in the main asteroid belt. Alternatively, Eros is not a product of a catastrophic disruption, and it formed with the planetesimals retaining, although fractured, its primordial interior structure. If so, its interior has been shattered by approximately a Solar System age worth of collisions to the point that its seismic properties are similar to those of a rubble pile.

A precise mapping of a quantitative value of Q to a qualitative description of the interior structure does not exist for asteroids. Here,

the inference for a rubble-pile interior is made on the basis of comparisons with terrestrial laboratory experiments and seismic investigations on the Moon and Mars⁴³, which show that the uppermost ‘coherent’ layer on these planetary surfaces is far less dissipative than our solution for Eros. If Eros is instead a heavily fractured but coherent asteroid, then our findings suggest that smaller rubble-pile asteroids are more dissipative by an additional order of magnitude, with $Q_T \approx 1$. This remaining ambiguity underscores the value that future seismic investigations at an asteroid would provide for understanding the origins and evolution of the population as a whole⁴².

By elucidating Q_T for asteroids, our findings enable tighter constraints on the rigidity and rheology of asteroids through telescopic observations of the tidal evolution of multiple systems². Future spacecraft visits to asteroids^{46,47} will provide an additional testbed for this type of analysis, which can provide further insight into the potential diversity of asteroid interiors.

Methods

Crater shape models

SPC. SPC is a well-established method of constructing shape models using images, and it has been used to generate both global DTMs of planetary objects⁴⁸ as well as local DTMs of geologic features of interest⁴⁹. The detailed workings of SPC are described in refs. 48,50. Here, we provide a brief description. To begin, a patch of surface, or maplet, surrounding a chosen landmark is modelled digitally to match images with a range of resolutions, incidence angles and emission angles. Cross-correlation of the imaging data with several views of the modelled maplet pinpoints the location of the landmark. Once many landmarks have been located in many images across a body, a linear minimization of the sum-squared residuals between the observed and modelled landmarks yields a solution for each landmark's position on the body, the spacecraft attitude, and the location and rotation of the body. Additional information is employed to improve this solution, such as the position of landmark maplets on the limbs of some images, correlations of adjacent maplets due to common topography and nominal spacecraft trajectory information.

The topographic modelling of each maplet takes advantage of two-dimensional photoclinometry and stereo effects. Observed brightness variations of a patch of surface are caused by albedo variations and the orientation of each surface element with respect to the sun and the camera. These variations constrain the slope and albedo at each maplet pixel using a linear minimization of the summed-square brightness residuals between the maplet and many images with different viewing geometries and illuminations. A Monte-Carlo integration allows the determination of local terrain heights relative to the landmarks. Height constraints from overlapping or lower-resolution maplets, limbs and geometric stereo are critical for deriving the normalized photometric function for image radiometry that relates slope to albedo, as no *a priori* function is assumed. The resulting normalized photometric function provides the basis for extrapolating the stereo-derived topography in low-resolution maplets to the high-resolution SPC topography.

The use of the SPC shape model allows the measurement of any profile across any crater on the surface of Eros, not limiting the dataset to those craters with NLR tracks through their centres. The highest-resolution global SPC shape model consists of 1.57 million vectors was constructed from MSI images²⁸; higher-resolution maplets that were used to derive the global shape model were used in this study to construct local DTMs (3 m ground sample distance) to measure crater diameter, depth and local slope, to get the highest possible resolution for the measurements. Supplementary Fig. 1 shows a comparison between an MSI image and an SPC local DTM of the 2.2-km-diameter crater Eurydice, depicting the quality of the SPC data.

Morphology measurements. The properties of the craters were measured by

- (1) mapping out the location of the crater rim using a rendered image of the topography and the high-resolution contours as a guide;
- (2) fitting an ellipse to the crater rim and using the mean of the ellipse dimensions to estimate a diameter and compute an estimate of the standard deviation;
- (3) fitting a plane to the mapped rim and using this plane and the diameter, computed in step 2, to measure the crater depth from the height above the plane;
- (4) estimating the uncertainty by using two rim fits: one for the 90% best fit rims height and one for the entire rim heights, giving a more representative error;
- (5) displaying contours on a DTM visualization and hand-picking the depth as the reasonable lowest point in the crater. This step was done by hand as numerical procedures may sometimes select a smaller crater within the crater being measured.

- We also measured crater dimensions through the use of crater profiles by
- (6) constructing eight profiles across the hand-picked crater centre;
 - (7) verifying the automatically detected crater rims by comparing their locations on the rendered image and with other profiles;
 - (8) selecting several representative profiles by hand to compute a profile-based diameter (this step was necessary to avoid the inclusion of profiles that were difficult to measure due to influence from the local topography, such as superposed craters and boulders);
 - (9) determining depths for each profile using the same procedure as step 5;
 - (10) reporting the mean geometric depths of each crater.

pkdgrav simulations of the fate of Shoemaker ejecta

We simulated the fate of ejecta from the Shoemaker-forming impact by combining ejecta scaling rules⁵¹ with direct *N*-body simulations of the gravitational and collisional dynamics of that ejecta using the code pkdgrav. pkdgrav is a highly parallelized *N*-body code capable of accurately simulating the gravitational and collisional interactions of *N* particles³².

We took the following steps to set up the simulations:

- (1) We created a representation of Eros in pkdgrav by using a low-resolution shape model²⁸ and ensuring that its mass, volume and density matched that of NEAR observations¹¹. The result is a rigid aggregate made out of ~20,000 spheres of equal mass.
- (2) We used a low-resolution three-dimensional shape model of Eros²⁸ and created an alpha shape of Shoemaker crater (see ref. 52 for alpha shape details) by selecting points on the crater rim.
- (3) The alpha shape is used to create a pre-Shoemaker-impact surface on Eros constructed out of pkdgrav particles, $N \approx 10,000$ spheres.
- (4) The Shoemaker particles are given ejection velocities based on ejecta scaling rules of ref. 51.

The ejection velocities of each pkdgrav particle, v_{ej} , at a distance r from the point of impact are calculated on the basis of the following formulation⁵¹:

$$v_{ej}(r) = C(gR)^{1/2} \left(\frac{r}{a}\right)^{-1/\mu_e} \left(1 - \frac{r}{n_2 R}\right)^p, \quad n_1 a \leq r \leq n_2 R, \quad (1)$$

where U is the impact speed, R is the crater radius, μ_e is a scaling parameter related to material properties, and the constants n_1 , n_2 and p are determined by fits to ejection velocity data. The values of $R = 3.25$ km. We set $U = 5.2$ km s⁻¹ based on the average main belt impact speed. $n_1 = 1.2$ and the values of $C = 0.55$, $\mu_e = 0.41$, $n_2 = 1.3$ and $p = 0.3$ are taken on the basis of experimental results of impacts on sand targets with 35% porosity. Additional simulations where $\mu_e = 0.35$ and 0.55 were performed to evaluate sensitivity of outcomes with μ_e .

- (1) With ejection velocities for Shoemaker defined, the spin properties of the entire asteroid, including Shoemaker particles, are modified. Here, we varied the spin period (4 h, 5.27 h, 8 h and no spin) to evaluate its influence on ejecta deposition.
- (2) The simulation is then allowed to run for 2 weeks of simulated time, which is much longer than expected crater formation timescale for Shoemaker (~10 min). More than 99% of the ejecta that are bound to Eros are reaccumulated at the end of each simulation.
- (3) Here, we are chiefly concerned with the gravitational dynamics of ejected particles around an irregularly shaped body and only track the initial reimpact location of each particle on the Eros body. pkdgrav particles may bounce or roll after impact, but,

as the simulated particles are large (~50 m diameter), we ignore this subsequent motion.

- (4) As the reimpact location of each particle is recorded, we can estimate the total depth of ejecta, d_{ej} , deposited at different locations on Eros by dividing the total volume of ejecta that impacts each facet of the shape model by that facet's surface area.
- (5) Crater degradation by ejecta emplacement is calculated by subtracting the ejecta volume deposited onto a crater with diameter, D , as $V_{cr,ej} = d_{ej}(\pi D^2/4)$, from the initial volume of that crater, V_{ini} , and then calculating the height of a paraboloid crater with volume $V_{ini} - V_{cr,ej}$.

Additional strength-scaled simulations were performed to evaluate ejecta deposition for a strength-controlled surface. The ejection velocities were scaled by a strength term, such that

$$v_{ej}(r) = C \left(\frac{Y}{\rho} \right)^{1/2} \left(\frac{r}{a} \right)^{-1/\mu_e} \left(1 - \frac{r}{n_2 R} \right)^p, \quad n_1 a \leq r \leq n_2 R, \quad (2)$$

where Y and ρ are the cratering strength and bulk density of the surface, respectively. Here, we assumed ρ was the same as the bulk density measured for Eros¹¹, based on measurements of Eros' relatively homogeneous gravity field.

Crater degradation model

We model the degradation of craters by first considering axially symmetric crater profiles. Following ref. 53, the initial depth, z_i , of an axially symmetric crater as a function of radial distance, r , from the crater centre can be analytically represented by

$$z_i(r) = \frac{dD^4}{128} \int_0^\infty k^3 \exp(-k^2 D^2/16) J_0(kr) dk, \quad (3)$$

where d is crater depth, D is crater diameter, J_0 is the zeroth-order Bessel function and k is the wavenumber. Any axially symmetric crater profile can be represented as an integral over a series of J_0 Bessel functions similar to how linear functions can be represented as a Fourier integral over sine and cosine functions.

We consider degradation of a crater due to impact-induced seismic shaking to proceed through the downslope diffusion of regolith²⁶. A general solution for the change in crater depth, z_f , as a function of radial distance is given by ref. 26 on the basis of techniques outlined in ref. 54:

$$z_f(r) = \frac{dD^4}{128} \int_0^\infty k^3 \exp(-k^2 D^2/16) J_0(kr) \exp(-Khk^2) dk, \quad (4)$$

which is similar to equation (3) except for the additional exponential term inside the integral $R = \exp(-Khk^2)$. This additional term, R , describes the influence of downslope diffusion events on the volume and morphology of the crater. K is the amount of downslope diffusion resulting from the impact, which quantifies the volume of material that is mobilized per unit area ($\text{m}^3 \text{m}^{-2}$), and h is the mobilized regolith thickness. For a constant impact energy (or seismic energy), a crater can be more easily erased for larger values of h (that is, thicker mobilized regolith layers). Similarly, the value of K depends on the energy of the impact such that more energetic impacts lead to stronger seismic shaking and more downslope diffusion of material. A demonstration of the use of these functional forms to model crater d/D is shown in Supplementary Fig. 2a.

A crater can be considered erased if it can no longer be detected due to a sufficiently shallow profile. From our survey of crater d/D , we find that this occurs when $d/D < 0.04$. We take half this value to be conservative in our analysis. This limit can be combined with the definition of R to obtain an estimate for the K required to erase a crater of a given

diameter, D , by setting $k = k_0 = 4/D$, the peak amplitude of the spatial waves. This gives a critical downslope diffusion value

$$K_c \geq \frac{1.3D^2}{16h}, \quad (5)$$

which can be rearranged to estimate the maximum crater size erased by a seismic wave that agitates the surface to a specific value of K :

$$D_{\max} = (16hK/1.3)^{1/2}. \quad (6)$$

We model the decay of the seismic wave by numerically solving for the value of K for each crater within the resurfaced region. In this manner, we can estimate how the value of K varies as a function of distance from the centre of the impact. We assume a value of $h = 1 \text{ m}$ (ref. 26), although this value for h only serves to scale the absolute value of K and has no bearing on our estimates of the seismic properties of Eros. For each crater, we perform the following Monte-Carlo simulation:

- (1) randomly assign the crater an initial d/D value based on the normal distribution of d/D values of craters of its size (Supplementary Fig. 2b);
- (2) numerically integrate equation (4) using the randomly drawn value of d/D as an input and using an initial guess at the value of K based on equation (5);
- (3) perform a gradient descent with updated values of K minimizing the difference, ε , between $z_f(0)$ and the measured depth of the crater;
- (4) once ε is less than some small tolerance value ($<10^{-4}$), save the value of K that produces $z_f(0) \approx d$;
- (5) repeat steps 1–4 49 more times to obtain an estimate on how the unknown initial d/D value of the crater influences the calculated K for the crater;
- (6) repeat steps 1–5, for each crater in our sample.

Seismic wave decay model

For impact-induced seismicity, we can define the following relationship between the impact energy, E_{imp} , and the total seismic energy, E_s , as follows:

$$E_s = \eta E_{\text{imp}}, \quad (7)$$

where η is the seismic efficiency, which describes the total amount of kinetic energy that is converted to seismic energy upon impact. Based on lunar seismology, η has been estimated to range between 10^{-6} and 10^{-4} . It has yet to be directly measured for an asteroid, although it has been estimated for the 1 km rubble-pile Ryugu to be $<10^{-6}$, based on image analysis of the region surrounding the artificial crater formed by the Small Carry-on Impactor released by Hayabusa2⁵⁵.

Here, we are concerned with attenuation of the surface seismic wave energy as it propagates to a distance, r , due to intrinsic absorption and scattering characteristics of the surface. For a Rayleigh wave, the attenuation factor, A_t , can be written as³³

$$A_t = \exp\left(\frac{-2\pi f r}{Q V_R}\right), \quad (8)$$

where f is the seismic wave frequency, V_R is the Rayleigh wave speed and ${}^E Q$ is the effective seismic quality factor, which depends on an intrinsic absorption quality factor, ${}^I Q_s$, and a scattering loss quality factor, ${}^{\text{sc}} Q$:

$$\frac{1}{{}^E Q} = \frac{1}{{}^I Q_s} + \frac{1}{{}^{\text{sc}} Q}. \quad (9)$$

In this manner, the total seismic energy decays as $E_S(r) = \eta E_{\text{imp}} A_r$. The scattering loss quality factor, $^{\text{Sc}}Q$, depends on frequency and seismic diffusivity, ξ (ref. 56):

$$^{\text{Sc}}Q = \frac{6\pi f \xi}{V_R^2}. \quad (10)$$

Values of 1Q for the lunar surface range from ~2,000 to 5,000 (refs. 57,58). $^{\text{Sc}}Q$ has not been measured independently of $^E Q$, but an $^E Q = 5$ has been measured for unconsolidated sand⁵⁹. Therefore, in the limit where $^1Q \gg ^{\text{Sc}}Q$, equation (9) shows that $^{\text{Sc}}Q = ^E Q$. We later independently show that this initial assumption is valid (Supplementary Information). In this manner, we can combine equations (7), (8) and (10) to show that

$$E_S(r) = \eta E_{\text{imp}} \exp\left(\frac{-r V_R}{3\xi}\right). \quad (11)$$

Finally, to compare our measured values of crater degradation to the seismic attenuation properties of the Eros surface, we consider the results of ref. 27, who performed a series of numerical simulations to understand the relationship between K and the properties of the impactor and target, finding the following prescription for K :

$$K \propto v_{\text{imp}}^{1/2} = (E_{\text{imp}})^{1/4}, \quad (12)$$

where v_{imp} is the impact speed. Combining equations (11) and (12), the attenuating properties of the Eros surface can be constrained from estimated values of K as

$$K(r) = K_0 \exp\left(\frac{-r}{\alpha}\right), \quad (13)$$

where $\alpha = 12\xi/V_R$ and K_0 is the value of K at $r = 0$, which captures the efficiency in transfer of kinetic impact energy to seismic energy. This solution provides a constraint on the scattering length as^{34,57}

$$\xi = V_R L_s / 3, \quad (14)$$

where L_s is the scattering length. Therefore, a measure of α directly determines L_s as substituting equation (14) into equation (11) shows that $\alpha = 4L_s$. Our observations of crater degradation allow us to estimate the value of K for craters as a function of distance, r , from the impact point, with the median values of K from our Monte Carlo simulation ('Crater degradation model' section in Methods), and the standard deviation of K for each crater as our uncertainty. Using a nonlinear least-squares regression technique⁶⁰, we fit our data to a function of the form shown in equation (13), which returns estimates for the value of K_0 and α . These values can then be subsequently used to estimate the maximum crater size erased as a function of distance, using equation (6).

Crater scaling relationships

Reference⁶¹ introduced generalized formulations of crater properties based on the Buckingham π theorem, which uses dimensionless numbers to estimate the crater volume, V_C , given impactor and target properties such as impactor the impactor radius, a , impactor velocity, U , impactor mass density, δ , target density, ρ , target strength, Y , and surface gravity, g . The π group parameters are related by

$$\pi_V = K_1 \left[\pi_2 \pi_4^{-1/3} + (K_2 \pi_3)^{(2+\mu_e)/2} \right]^{-3\mu_e/(2+\mu_e)} \quad (15)$$

and

$$\pi_V = \frac{\rho V_C}{m_{\text{imp}}} = \frac{\rho (R_C/K_r)^3}{m_{\text{imp}}}, \quad (16)$$

where m_{imp} is the projectile mass and R_C is the crater radius. K_r , K_2 , K_r and μ_e are crater scaling constants that depend on the target material. K_r relates the radius of the crater to its volume. The π -group parameters that control the cratering efficiency, π_v , are

$$\pi_2 = \frac{ga}{U^2} \quad (17)$$

$$\pi_3 = \frac{Y}{\rho U^2} \quad (18)$$

$$\pi_4 = \frac{\rho}{\delta}. \quad (19)$$

Here, we are interested in the cratering efficiency for Shoemaker crater. Based on our observation of $d/D \approx 0.2$ for the largest craters on Eros, we set $K_r = 1.2$ and generally $K_2 = 1$. We assume $\delta = 3 \text{ g cm}^{-3}$, $\rho = 2.7 \text{ g cm}^{-3}$ and $g = 5 \text{ mm s}^{-2}$. For the gravity-dominated case, we consider the results stemming from the small carry-on impactor experiment on 1 km rubble-pile Ryugu, part of the Hayabusa2 mission, which determined that $K_1 \approx 0.15$, and $\mu_e = 0.41$ (ref. 6). We also show that $\mu_e = 0.41$ is consistent with the crater degradation pattern seen on the Shoemaker antipode as replicated in our ejecta simulations that area described in the main text and Supplementary Information. Note that their in-text formulation of the π -scaling laws neglects K_r , leading to a different quoted value of K_1 . For the strength-dominated case, we consider the material properties of dry soil⁶², which has $Y = 0.18 \text{ MPa}$, $K_1 = 0.24$ and $\mu_e = 0.41$.

Data availability

MSI images and NLR data from the NEAR mission are available in the Planetary Data System Small Bodies Node hosted by the University of Maryland (https://pds-smallbodies.astro.umd.edu/data_sb/missions/near/index.shtml). The DTMs analysed here are available in a permanent archive associated with this paper in the JHU/APL Data Archive. Measured diameters, depths, d/D , associated uncertainties and locations of craters are available in Supplementary Table 1.

Code availability

The Small Body Mapping Tool is a publicly available mapping toolset that is available through the software's website (<http://sbmt.jhuapl.edu/>).

References

- Chapman, C. R. et al. Cratering on Mathilde. *Icarus* **140**, 28–33 (1999).
- Nimmo, F. & Matsuyama, I. Tidal dissipation in rubble-pile asteroids. *Icarus* **321**, 715–721 (2019).
- Asphaug, E. Interiors of small bodies and moons. *Nat. Commun.* **11**, 1564 (2020).
- Walsh, K. J. Rubble pile asteroids. *Annu. Rev. Astron. Astrophys.* **56**, 593–624 (2018).
- Prockter, L. et al. Surface expression of structural features on Eros. *Icarus* **155**, 75–93 (2002).
- Arakawa, M. et al. An artificial impact on the asteroid (162173) Ryugu formed a crater in the gravity-dominated regime. *Science* **368**, 67–71 (2020).
- Tricarico, P. et al. Internal rubble properties of asteroids (101955) Bennu. *Icarus* **370**, 114665 (2021).
- Chapman, C. R. et al. Impact history of Eros: craters and boulders. *Icarus* **155**, 104–118 (2002).
- Robinson, M. S. et al. The geology of 433 Eros. *Meteorit. Planet. Sci.* **37**, 1651–1684 (2002).
- Buczkowski, D. L. et al. 433 Eros lineaments: global mapping and analysis. *Icarus* **193**, 39–52 (2008).

11. Yeomans, D. K. et al. Radio science results during the NEAR-Shoemaker spacecraft rendezvous with Eros. *Science* **289**, 2085–2088 (2000).
12. Flynn, G. J. et al. Physical properties of the stone meteorites: implications for the properties of their parent bodies. *Geochemistry* **78**, 269–298 (2018).
13. Peplowski, P. N. et al. Hydrogen and major element concentrations on 433 Eros: evidence for an L- or LL-chondrite-like surface composition. *Meteorit. Planet. Sci.* **50**, 353–367 (2015).
14. Wilkison, S. L. et al. An estimate of Eros's porosity and implications for internal structure. *Icarus* **155**, 94–103 (2002).
15. Tonge, A. L. et al. A model for impact-induced lineament formation and porosity growth on Eros. *Icarus* **266**, 76–87 (2016).
16. Fujiwara, A. et al. The rubble-pile asteroid Itokawa as observed by Hayabusa. *Science* **312**, 1330–1334 (2006).
17. Sugita, S. et al. The geomorphology, color, and thermal properties of Ryugu: implications for parent-body processes. *Science* **364**, eaaw0422 (2019).
18. Walsh, K. J. et al. Craters, boulders and regolith of (101955) Bennu indicative of an old and dynamic surface. *Nat. Geosci.* **12**, 242–246 (2019).
19. Terada, K. et al. Thermal and impact histories of 25143 Itokawa recorded in Hayabusa particles. *Sci. Rep.* **8**, 11806 (2018).
20. Nakamura, T. et al. Formation and evolution of carbonaceous asteroid Ryugu: direct evidence from returned samples. *Science* **379**, abn8671 (2022).
21. Pravec, P. et al. in *Asteroids III* (eds Bottke, W. F. Jr et al.) 113–122 (Univ. Arizona Press, 2002).
22. Delbo, M. et al. Identification of a primordial asteroid family constrains the original planetesimal population. *Science* **357**, 1026–1029 (2017).
23. Grott, M. et al. Macroporosity and grain density of rubble pile asteroid (162173) Ryugu. *J. Geophys. Res. Planets* **125**, e2020JE006519 (2020).
24. Stickle, A. M. et al. Modeling momentum transfer from kinetic impacts: implications for redirecting asteroids. *Procedia Eng.* **130**, 577–583 (2017).
25. Thomas, P. C. & Robinson, M. S. Seismic resurfacing by a single impact on the asteroid 433 Eros. *Nature* **436**, 366–369 (2005).
26. Richardson, J. E. et al. The global effects of impact-induced seismic activity on fractured asteroid surface morphology. *Icarus* **179**, 325–349 (2005).
27. Richardson, J. E. et al. Impact-produced seismic shaking and regolith growth on asteroids 433 Eros, 2867 Šteins, and 25143 Itokawa. *Icarus* **347**, 113811 (2020).
28. Gaskell, R. W. Gaskell Eros Shape Model V1.0. NEAR-A-MSI-5-EROSHAPE-V1.0. NASA Planetary Data System <https://doi.org/10.26033/dOgq-9427> (2008).
29. Pike, R. J. Apparent depth/apparent diameter relation for lunar craters. In *Proc. 8th Lunar Science Conference* 3427–3436 (Pergamon Press, 1977).
30. Marchi, S. et al. in *Asteroids IV* (eds Michel, P. et al.) 725–744 (Univ. of Arizona, 2015).
31. Thomas, P. C. et al. Shoemaker crater as the source of most ejecta blocks on the asteroid 433 Eros. *Nature* **413**, 394–396 (2001).
32. Richardson, D. C. et al. Direct large-scale *N*-body simulations of planetesimal dynamics. *Icarus* **143**, 45–59 (2000).
33. Aki, K. & Richards, P. G. *Quantitative Seismology* 2nd edn (University Science Books, 1969).
34. Toksöz, M. N. et al. Structure of the moon. *Rev. Geophys. Space Phys.* **12**, 539–567 (1974).
35. Lognonné, P. et al. Moon meteoritic seismic hum: steady state prediction. *J. Geophys. Res.* **114**, E12003 (2009).
36. Ammon, C. J. et al. *Foundations of Modern Global Seismology* 2nd edn, 39–63 (Academic, 2021).
37. Onodera, K. et al. Seismic scattering and absorption properties of Mars estimated through coda analysis on a long-period surface wave of S1222a Marsquake. *Geophys. Res. Lett.* **50**, e2022GL107216 (2023).
38. Goldreich, P. & Sari, R. Tidal evolution of rubble piles. *Astrophys. J.* **691**, 54–60 (2009).
39. Lekic, V. et al. Measurement and implications of frequency dependence of attenuation. *Earth Planet. Sci. Lett.* **282**, 285–293 (2009).
40. Pou, L. et al. Tidal constraints on the Martian interior. *J. Geophys. Res. Planets* **127**, e2022JE007291 (2022).
41. Brož, M. et al. Observed tidal evolution of Kleopatra's outer satellite. *Astron. Astrophys.* **657**, A76 (2022).
42. DellaGiustina, D. N. et al. Seismology of rubble-pile asteroids in binary systems. *Mon. Not. R. Astron. Soc.* **528**, 6568–6580 (2024).
43. Frankel, A. & Clayton, R. W. Finite difference simulations of seismic scattering: Implications for the propagation of short-period seismic waves in the crust and models of crustal heterogeneity. *J. Geophys. Res.* **91**, 6465–6489 (1986).
44. Cheng, B. et al. Numerical simulations of drainage grooves in response to extensional fracturing: testing the Phobos groove formation model. *Planet. Sci. J.* **3**, 249 (2022).
45. Barnouin, O. S. et al. Shape of (101955) Bennu indicative of a rubble pile with internal stiffness. *Nat. Geosci.* **12**, 247–252 (2019).
46. Levison, H. F. et al. Lucy mission to the Trojan asteroids: science goals. *Planet. Sci. J.* **2**, 171 (2021).
47. DellaGiustina, D. N. et al. OSIRIS-APEX: an OSIRIS-REx extended mission to asteroid Apophis. *Planet. Sci. J.* **4**, id.198, 22pp. (2023).
48. Gaskell, R. W. et al. Characterizing and navigating small bodies with imaging data. *Meteorit. Planet. Sci.* **43**, 1049–1061 (2008).
49. Daly, R. T. et al. The morphometry of impact craters on Bennu. *Geophys. Res. Lett.* **47**, e89672 (2020).
50. Gaskell, R. W. et al. Stereophotoclinometry on the OSIRIS-REx mission: mathematics and methods. *Planet. Sci. J.* **4**, 63 (2023).
51. Housen, K. R. & Holsapple, K. A. Ejecta from impact craters. *Icarus* **211**, 856–875 (2011).
52. Ballouz, R.-L. et al. Using a geometrical algorithm to provide *N*-body initial conditions for the gravitational phase of asteroid family formation. *Mon. Not. R. Astron. Soc.* **485**, 697–707 (2019).
53. Melosh, H. J. *Impact Cratering: A Geologic Process* (Oxford Univ. Press 1989).
54. Kreyszig, E. *Advanced Engineering Mathematics* (John Wiley & Sons, 1993).
55. Nishiyama, G. et al. Simulation of seismic wave propagation on asteroid Ryugu induced by the impact experiment of the Hayabusa2 mission: limited mass transport by low yield strength of porous regolith. *JGR Planets* **126**, e06594 (2021).
56. Sato, H., Fehler, M. C., & Maeda, T. *Seismic Wave Propagation and Scattering in the Heterogeneous Earth* (Springer, 2012).
57. Dainty, A. M. et al. Seismic scattering and shallow structure of the Moon in oceanus procellarum. *Moon* **9**, 11–29 (1974).
58. Nakamura, Y. Seismic energy transmission in the lunar surface zone determined from signals generated by movement of Lunar Rovers. *Bull. Seismol. Soc. Am.* **66**, 593–606 (1976).
59. Daubar, I. et al. Impact-seismic investigations of the InSight mission. *Space Sci. Rev.* **214**, 132 (2018).
60. Virtanen, P. et al. SciPy 1.0: fundamental algorithms for scientific computing in Python. *Nat. Methods* **17**, 261–272 (2020).
61. Holsapple, K. A. & Schmidt, R. M. Point source solutions and coupling parameters in cratering mechanics. *J. Geophys. Res.* **92**, 6350–6376 (1987).
62. Holsapple, K. A. & Housen, K. R. A crater and its ejecta: an interpretation of deep impact. *Icarus* **191**, 586–597 (2007).

63. Chabot, N. C. et al. MEGANE investigations of Phobos and the Small Body Mapping Tool. *Earth Planets Space* **73**, 217 (2021).
64. Stooke, P. Stooke *Small Bodies Maps V3.0. MULTI-SA-MULTI-6-STOOKEMAPS-V3.0* (NASA Planetary Data System, 2015)

Acknowledgements

R.-L.B., C.M.E., O.S.B. and R.T.D. acknowledge support from the NASA Discovery Data Analysis Program under grant 80NSSC20K1154 to O.S.B.

Author contributions

R.-L.B., C.M.E. and O.S.B. contributed to the conceptualization of the study. O.S.B. formulated the concept of using crater degradation as a tracer of near-surface processes. C.M.E. and O.S.B. contributed to the construction of Eros crater DTMs. O.S.B., R.T.D. and R.-L.B. contributed to the crater morphological analysis software. C.M.E., R.-L.B., B.A.H. and A.C.M. contributed to the morphological analysis of craters. R.-L.B. led the analysis associated with ejecta emplacement and seismic shaking. R.-L.B., C.M.E., O.S.B., R.T.D. and D.N.D. contributed to the interpretation of results. R.-L.B. and C.M.E. contributed to drafting the manuscript. R.-L.B., C.M.E., O.S.B., R.T.D. and D.N.D. contributed to revising the manuscript.

Competing interests

The authors declare no competing financial interests.

Additional information

Extended data is available for this paper at <https://doi.org/10.1038/s41550-024-02411-8>.

Supplementary information The online version contains supplementary material available at <https://doi.org/10.1038/s41550-024-02411-8>.

Correspondence and requests for materials should be addressed to R.-L. Ballouz.

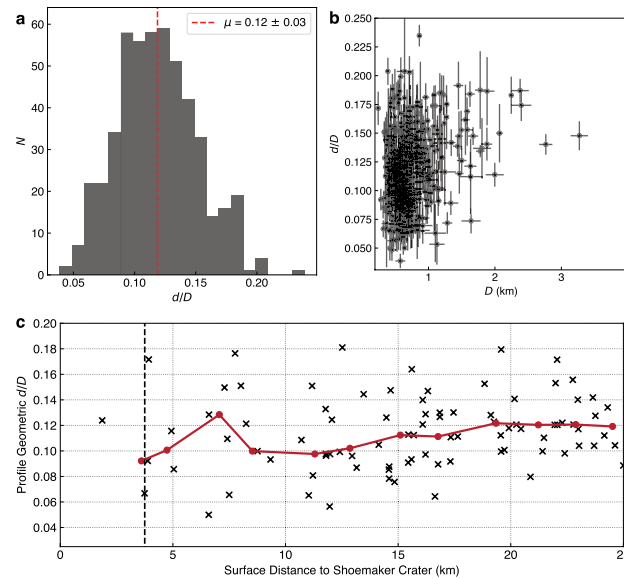
Peer review information *Nature Astronomy* thanks Mark Panning, David Polishook and the other, anonymous, reviewer(s) for their contribution to the peer review of this work.

Reprints and permissions information is available at www.nature.com/reprints.

Publisher's note Springer Nature remains neutral with regard to jurisdictional claims in published maps and institutional affiliations.

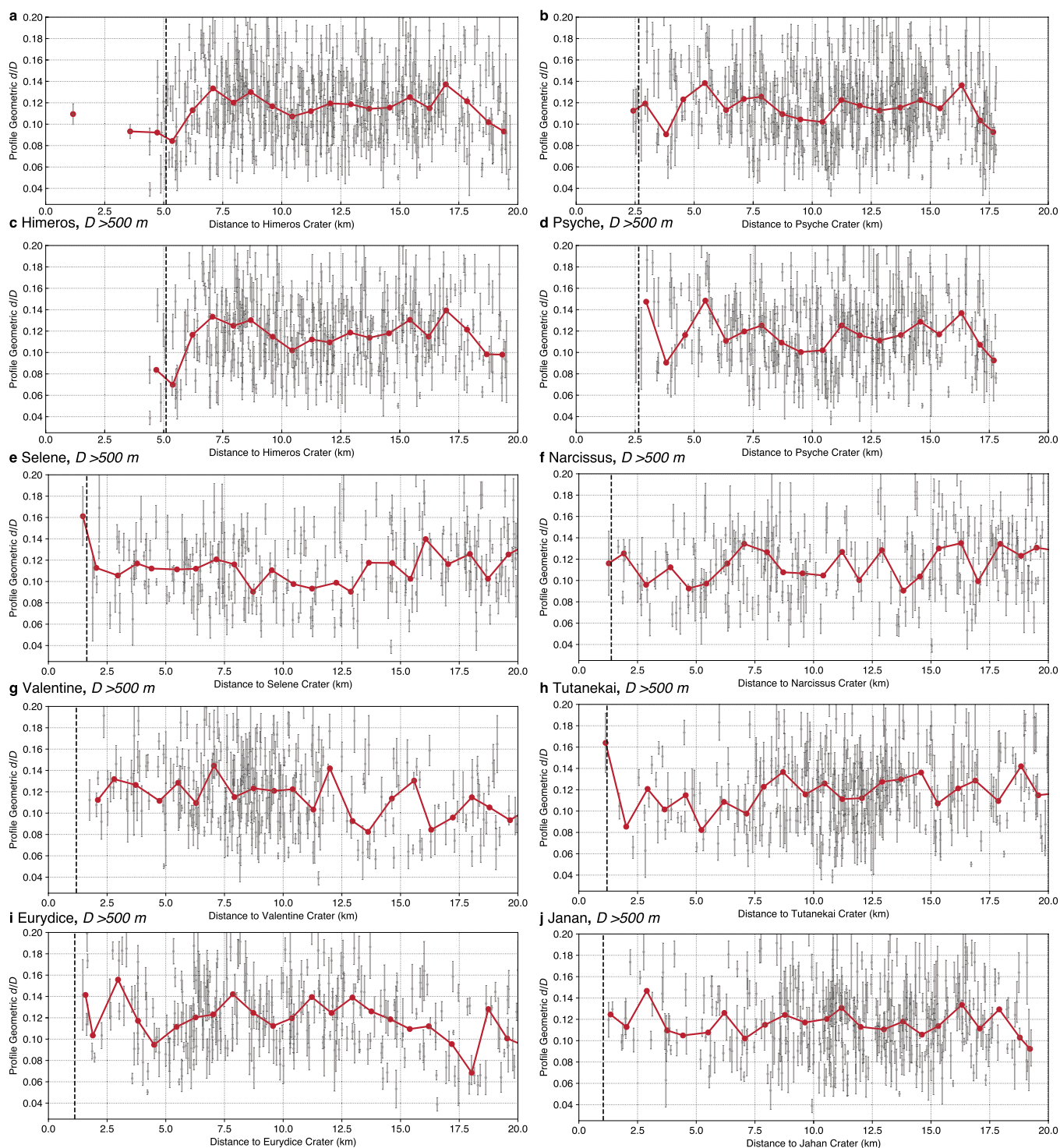
Open Access This article is licensed under a Creative Commons Attribution-NonCommercial-NoDerivatives 4.0 International License, which permits any non-commercial use, sharing, distribution and reproduction in any medium or format, as long as you give appropriate credit to the original author(s) and the source, provide a link to the Creative Commons licence, and indicate if you modified the licensed material. You do not have permission under this licence to share adapted material derived from this article or parts of it. The images or other third party material in this article are included in the article's Creative Commons licence, unless indicated otherwise in a credit line to the material. If material is not included in the article's Creative Commons licence and your intended use is not permitted by statutory regulation or exceeds the permitted use, you will need to obtain permission directly from the copyright holder. To view a copy of this licence, visit <http://creativecommons.org/licenses/by-nc-nd/4.0/>.

© The Author(s) 2024



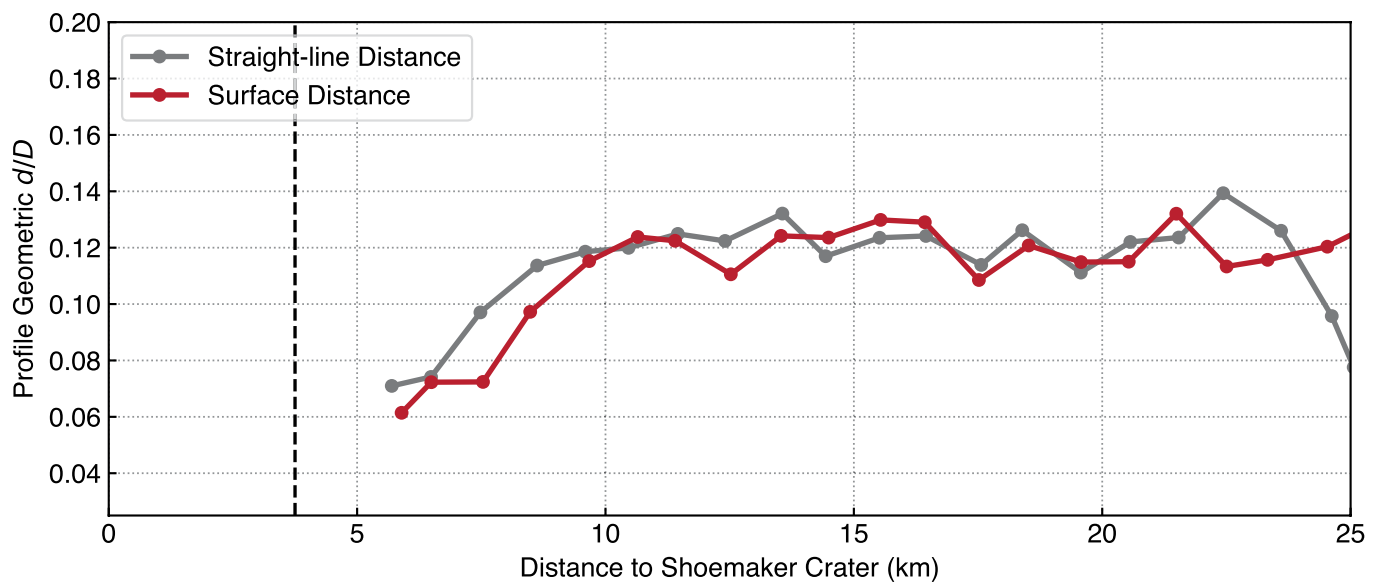
Extended Data Fig. 1 | Population-wide properties of Eros crater depth-to-diameter ratios, d/D . **a**, Histogram showing the global distribution of crater depth, d , to diameter, D , ratio, d/D . The d/D of 500 craters on Eros have a mean value of 0.12 and a 1-sigma standard deviation of 0.03 (shown by the vertical dashed red line). **b**, The distribution of crater d/D as a function of D . There is a larger spread in d/D values at smaller sizes, and craters 500–1000 m in

diameter exhibit the largest degree of degradation. The circles show the mean $d/D \pm 1$ -sigma standard deviation of craters. The number of profiles used to calculate the standard deviation in d/D ranges from 3 to 8. **c**, The d/D of craters with $D < 500$ m (black crosses) as a function of surface distance to Shoemaker. The red curve shows the moving average (median) of the black crosses. No clear trend exists for smaller ($D < 500$ m) craters compared to larger craters (Fig. 2a).



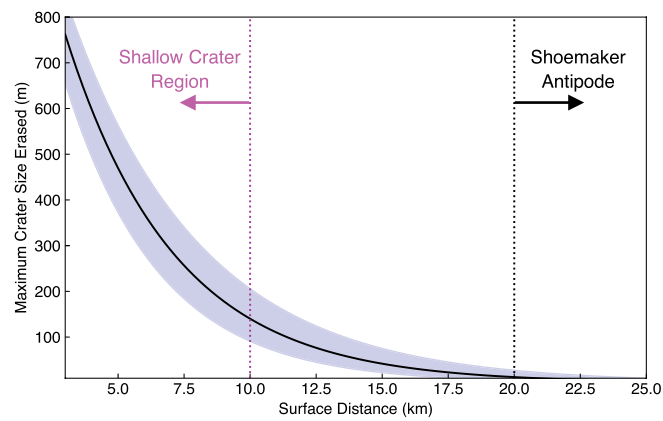
Extended Data Fig. 2 | Trends in d/D with distance for other large craters (> 2 km) on Eros. The red curve in each panel shows the moving average (median) of the grey circles. The grey circles in each panel represent the mean $d/D \pm 1$ standard deviation of craters. The number of profiles used to calculate the standard deviation in d/D ranges from 3 to 8. The vertical black dashed line marks a distance of one radius from the reference crater. Unlike Shoemaker crater

(Fig. 1a), no trends between d/D and distance to the other craters are apparent. **a**, d/D of all craters as a function of distance to Himeros crater. **b**, d/D of all craters as a function of distance to Psyche crater. **c–j**, d/D of craters with $D > 500$ m, as a function of distance to **c**, Himeros crater, **d**, Psyche crater, **e**, Selene crater, **f**, Narcissus crater, **g**, Valentine crater, **h**, Tutanekai crater, **i**, Eurydice crater, and **j**, Jahan crater.



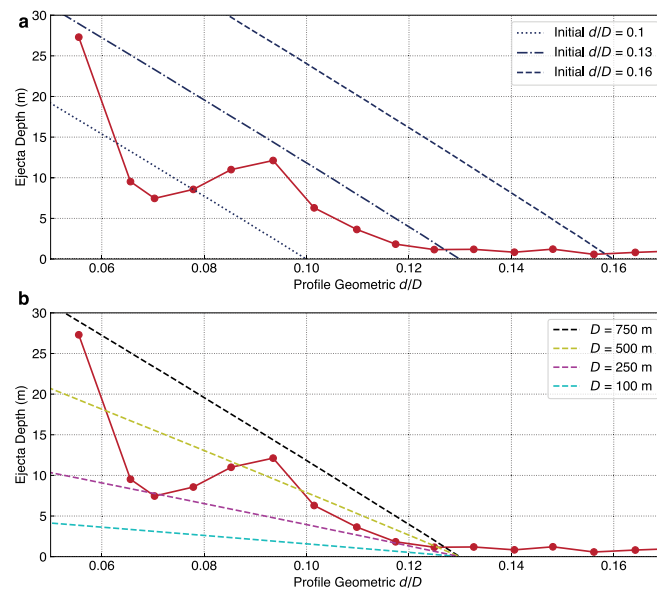
Extended Data Fig. 3 | Crater d/D increases as a function of distance from the center of Shoemaker crater. Median crater d/D as a function of surface distance (red curve) and straight-line distance (grey curve) from the center of Shoemaker crater, showing an increase in d/D with both surface and straight-line distance from Shoemaker, similar to crater R (Fig. 2b,c). The trend is more prominent in

surface distance (red curve) and shifted rightward compared to straight-line distance (grey curve). We find that both the median values of crater R and d/D with distance to Shoemaker crater asymptote at larger surface-distances compared to straight-line distances. The vertical black dashed line marks one Shoemaker crater radius.



Extended Data Fig. 4 | The maximum crater size erased by our modeled surface seismic wave as a function of distance. The black solid line represents our nominal solution, and the blue shaded region shows the model's 1-sigma uncertainties that is centered on the modeled curve. Craters with $D < 250$ m

within the entire *Shallow Crater Region* are erased by the surface seismic wave alone. At the antipode, only craters with $D < 10$ m could have been erased by the surface seismic wave.



Extended Data Fig. 5 | The depth of simulated ejecta as a function of the d/D of craters at the same location on Eros. **a, there is an expected negative correlation between ejecta depth and crater d/D for deeper craters with $d/D = 0.09$ – 0.12 , but this trend is less clear for shallower craters with $d/D < 0.09$. The dashed, dot-dashed, and dotted blue curves correspond to the ejecta depth**

required to degrade a 750-m diameter crater with initial $d/D = 0.16$, 0.13 , and 0.10 , respectively. **b**, same as **a**, but varying the size of the crater and keeping constant the initial $d/D = 0.13$. Ejecta deposition may feasibly be responsible for the degradation of craters with $D < 250$ m, but a different mechanism is required for larger craters.

Extended Data Table 1 | A matrix of Eros geologic observations that can be explained with a given mechanism or combination of mechanisms

<div>Mechanism</div> <div>Observation</div>	Body Waves (BW)	Surface Waves (SW)	Ejecta	BW + Ejecta	SW + Ejecta	BW + SW
SCR Small Crater R	no	yes	no	no	yes	yes
SCR Large Crater d/D	no	yes	no	no	yes	yes
Antipode Small Crater R	partial	no	yes	yes	yes	partial
Antipode Large Crater d/D	partial	yes	yes	yes	yes	partial
Antipode Chevron Pattern	partial	no	yes	yes	yes	partial

The transition between small and large craters is at approximately 500m. The observations and modeling suggest that this demarcation is not so starkly defined and there exists a transition region between 250 and 500m. However, for the purposes of this exercise, it is useful to define a clear transition where the differences in geologic properties are clearly observed.

Extended Data Table 2 | Summary of *pkdgrav* ejecta deposition simulation cases and outcomes

Case	μ_e	Scaling	Material	P (h)	f_{ret}	V_{ret} (km ³)
1	0.35	Gravity	Sand	5.27	0.35	5.72
2	0.41	Gravity	Sand	5.27	0.41	6.67
3	0.55	Gravity	Sand	5.27	0.54	8.73
4	0.41	Gravity	Sand	no spin	0.45	7.26
5	0.41	Gravity	Sand	4	0.40	6.47
6	0.41	Gravity	Sand	8	0.43	6.94
7	0.46	Strength 0.10 MPa	WCB	5.27	0.32	5.21
8	0.46	Strength 0.45 MPa	WCB	5.27	0.11	1.72
9	0.55	Strength 30 MPa	Rock	5.27	<0.01	0.02

The ejection scaling parameter, μ_e , was varied between 0.35–0.55, with a nominal value of 0.41. P = rotation period, f_{ret} = fraction of escaped ejecta, V_{ret} = volume of retained ejecta. Properties of different materials are described in the Supplementary Information.